A UV to NIR Si Wavelength Sensor With Simple Geometry and Good Resolution

Can Fu, Chuan Lu, Hai-Yang Cheng, Xiang Zhang, Zhi-Xiang Zhang, Yu-Tian Xiao, Di-Hua Lin, Jiang Wang, Ji-Gang Hu, *Member, IEEE*, Zhi-Li Wang, Di Wu, and Lin-Bao Luo, *Senior Member, IEEE*

***Abstract*— In this work, a wavelength sensor that is capable of quantitatively distinguishing the wavelength in the range of ultraviolet (UV) to near-infrared (NIR) light (265–1050 nm) is presented. The wavelength sensor is fabricated by depositing two parallel Au electrodes on the two sides of a 200 μm Si wafer. It is found that the as-formed two photodetectors display completely different optical properties. And then, the relationship between the photocurrent ratio of two photodetectors and incident wavelength can be described as a numerical function, through which the wavelength from 265 to 1050 nm can be precisely calculated. The unique operation mechanism of the Si wavelength sensor is unveiled by technology computer-aided design (TCAD) simulation. Remarkably, the wavelength sensor easily distinguishes the light with a wavelength difference of 1 nm, which is much better than previously reported devices based on the vertically stacked structures and charge collection narrowing mechanism.**

***Index Terms*— Distribution of photocurrent rate, monotonic function, Schottky junction, Si wavelength sensor.**

I. Introduction

A WAVELENGTH sensor is a kind of optoelectronic device that can distinguish different wavelengths of light illumination quantitively [1]–[5]. As a complement to imaging sensors [6], [7], wavelength sensors have recently received extensive attention for their promising applications in the field of security monitor, lab-in-a-phone, self-driving, drones, and remote-sensing technologies [3], [8]–[13]. For example, wavelength sensors are often used to detect the color and position of an object in the field of safety monitoring, which can realize accurate tracking [3].

To date, very few studies about the wavelength sensor have been reported, except for some conventional devices based on the following geometries [2]–[5], [13]. Traditional spectral discrimination methods of early reports adopt complex optical structure systems, such as diffraction grating, prisms, etc. [14], [15]. The optical dispersion usually needs additional physical space leading to the increase of volume. Therefore, optical filter arrays combined with broadband photodetectors are proposed to pursue miniaturization, called filter-assisted wavelength sensors [16]–[18]. However, the optical gadget could cause photon loss due to the absorption or reflection of the filter, limiting the detection efficiency and spectral range [17]. Subsequently, filter-free wavelength sensors are investigated and developed, like the vertically stacked structures, employing narrowband materials and nanostructural photodetector arrays [2], [4], [13], [19]. These are suitable for assembling spectrometers to achieve miniaturization and light, while most of these devices have a narrow detection range or unsatisfactory wavelength resolution [2], [19].

To solve these problems, we proposed a new simple geometry silicon wavelength sensor that is able to determine the wavelength in the range of ultraviolet (UV) to near-infrared (NIR) (265–1050 nm). In particular, the resolution is as low as 1 nm in the wavelength range of 450–900 nm.

II. Experimental Details

A. Device Fabrication

To fabricate the Au/Si/Au photodetectors-based wavelength sensor, the n-type (100) Si wafer (resistivity: 1–10 Ω·cm, two sides polished) was cut into appropriate pieces with a size of 0.5 × 1 cm^2, and then etched in a buffered oxide etch solution (HF: NH_4F: H_2O = 3:6:10) for 2 min to remove the oxide layer. Subsequently, it was ultrasonically cleaned in sequence with acetone, ethanol, and deionized water for 30 min. A positive photoresist layer was spin-coated on the Si substrate, followed by defining an interdigital electrode pattern through a UV photolithography process, during which two adjacent edges of the silicon wafer were chosen as reference to align with the cross of the lithography mask. After that, 50 nm-thick Au layers were coated onto the Si substrate using electron beam evaporation processes, and the photoresist was removed with acetone. The gold layer was directly deposited, which displayed good adhesion with the Si wafer due to

Manuscript received January 28, 2022; accepted March 17, 2022. Date of publication March 30, 2022; date of current version April 22, 2022. This work was supported in part by the National Natural Science Foundation of China under Grant 62074048, Grant 62075053, and Grant U20A20216; in part by the Fundamental Research Funds for the Central Universities under Grant JZ2018HGXC0001 and Grant PA2020GDKC0024; and in part by the Open Foundation of Anhui Provincial Key Laboratory of Advanced Functional Materials and Devices under Grant 4500-411104/011. The review of this article was arranged by Editor R. Kuroda. *(Corresponding author: Lin-Bao Luo.)*

Can Fu, Chuan Lu, Hai-Yang Cheng, Xiang Zhang, Zhi-Xiang Zhang, Jiang Wang, and Lin-Bao Luo are with the School of Microelectronics, Hefei University of Technology, Hefei 230009, China (e-mail: luolb@hfut.edu.cn).

Yu-Tian Xiao, Di-Hua Lin, Ji-Gang Hu, and Zhi-Li Wang are with the School of Physics, Hefei University of Technology, Hefei, Anhui 230009, China.

Di Wu is with the School of Physics and Engineering and Key Laboratory of Material Physics of Ministry of Education, Zhengzhou University, Zhengzhou, Henan 450052, China.

Color versions of one or more figures in this article are available at https://doi.org/10.1109/TED.2022.3161253.

Digital Object Identifier 10.1109/TED.2022.3161253

the relatively slow deposition rate during the electron beam evaporation [20]. Then polymethyl methacrylate (PMMA) used as a protection layer was spin-coated on Au interdigital electrode. The back interdigital electrode on the other side of Si was prepared by the same method. Notably, the marking edge should be aligned again to make sure both back and front photodetectors are symmetrical. Finally, the PMMA protection layer and photoresist are removed together with acetone.

B. Device Characterization and Device Simulation

The optoelectronic property of an individual photodetector and the wavelength sensor were investigated by a semiconductor characterization system (4200-SCS, Keithley Company Ltd.) equipped with a monochromator (SP2150, Princeton Company). Illumination with constant intensity is obtained by tailoring the slit width of the monochromator. It is worth noting that the monochromator has been calibrated before characterization. And its resolution is 0.25 nm, which is good enough to ignore the influence of the incident light width. Before device analysis, the power intensity of the incident light was calibrated by a power meter (Thorlabs GmbH, PM 100D). What is more, the electrode fingers were studied by scanning electron microscopy (SEM, KYKY-6900). During the Synopsys Sentaurus technology computer aided design (TCAD) calculation, wavelength sensors consisting of n-type (100) Si wafer (the thick range from 100 to 650 μm; doping level: 10^{15} cm^{-3}) were considered. During simulation, a beam of light was vertically shined on the device with an intensity of 1 mW/cm^2.

III. Results and Discussion

The proof-of-concept wavelength sensor was realized with a metal–semiconductor–metal (MSM) structure, forming two photodetectors on the front and back surfaces of Si substrate [see Fig. 1(a)]. For convenience, the incident side of light is defined as the front surface, and the photodetector on this surface is named as PD1. The other side of the Si substrate is defined as the back surface, and the photodetector is marked as PD2. The inset of Fig. 1(a) displays an SEM image of the interdigital electrodes. The electrode fingers were 200 μm wide with 200 μm spacing gaps. The reason why Au was used as the electrode is Au metal can form an ideal Schottky junction with n-type Si [20]. The upper right pink shaded area in Fig. 1(b) shows the depletion region at 1 V bias. In this work, two photodetectors were separately measured to obtain the photocurrent (the current under light illumination minus the dark current) ratio. The depletion layer depends on the applied voltage, and therefore the corresponding width of the built-in electric field on both sides are different: The width of the depletion region with 1 V bias (W_1) is calculated to be about 1.6 μm [inset of Fig. 1(b)], while the width of the depletion region without bias (W_2) is around 1 μm. According to our calculation, the diffusion length (L) corresponding to the present n-type Si (mobility: 500 cm^2/V·s) was estimated to be 316 μm [5], suggesting that two photodetectors will share the diffusion region when the thickness of Si is less than 635.2 μm [$635.2 = 2L + W_1 + W_2$]. Then the thickness of Si substrate will significantly affect the performance of

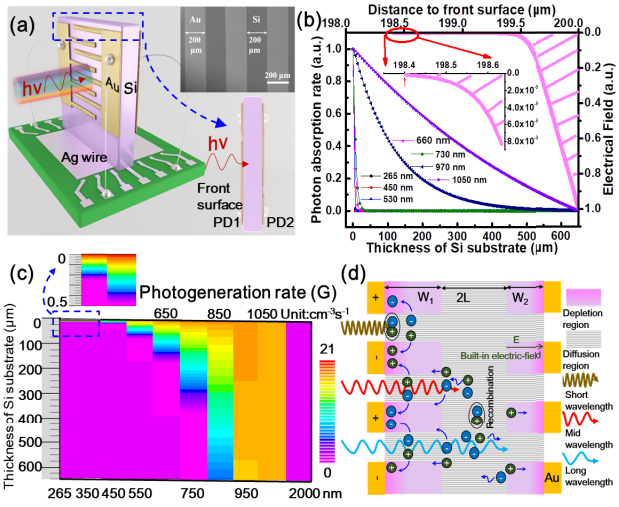

Fig. 1. (a) Schematic illustration of wavelength sensor with Au/n-Si/Au structure. Inset: SEM image of interdigital electrodes. (b) Electrical field and normalized photon absorption rate versus distance to the front surface. (c) Photogeneration rate of 265–1050 and 2000 nm light in 650 μm thicknesses Si substrate. (d) Schematic of the wavelength sensor based on Si Schottky junctions.

the wavelength sensor, so it is discussed in detail. Fig. 1(b) displays the curve of the simulated normalized photon absorption rate with Si substrate thickness. Obviously, the photon absorption rates decrease almost sharply when the incident light wavelength is shorter than 970 nm, which means most of the short wavelength photons are only absorbed in front surface. This is in sharp contrast with the photon absorption rate distribution under 970 and 1050 nm light illumination. The long wavelength is absorbed in the whole Si substrate due to a slow attenuation trend of photon absorption rate. Therefore, the unique distribution of photon absorption rate makes the two photodetectors may have completely different photoelectric characteristics.

TCAD simulation on the photogeneration rate (G) of wavelength sensor was performed under 265–1050 and 2000 nm light illuminations, as depicted in Fig. 1(c). For the illumination of short wavelengths, the G is concentrated in the depletion region of PD1. With the gradual increase of wavelength, the G region gradually extends from the front surface to the deep thickness of the wavelength sensor. It means that the transmission depth of incident light increases with the increase of wavelength. When the wavelength is close to 850 nm, electron-hole pairs (EHPs) will be generated at a depth of 650 μm. It is worth noting that G will reduce when the wavelength is too long because the irradiation energy is lower than the Si bandgap, like G under 2000 nm incident light. Fig. 1(d) illustrates EHPs under the illumination of short, mid, and long wavelengths. Here, the thickness of Si substrate was selected to be 635.2 μm. Under light illumination, the wavelength sensor can be divided into two depletion regions and two diffusion regions. Then short wavelength incident light was only absorbed by PD1 to generate EHPs, forming photocurrent in PD1. With the incident light wavelength increasing, the generations of EHPs gradually extend from the PD1 to the PD2. For long wavelength incident light, it was absorbed by PD1 and PD2 to generate EHPs, forming photocurrent in those

two photodetectors. Consequently, two photodetectors should exhibit two different photoresponses when the incident lights with different wavelengths illuminate from the front.

Next, the photocurrent distributions of PD1 and PD2 with different thicknesses Si were simulated using TCAD at 1 V bias voltage [see Fig. 2(a)]. The simulated photocurrents of PD1 and PD2 are marked as $I_{S,1}$ and $I_{S,2}$, respectively. The PD1s offer broadband photoresponse from 265 to 1200 nm, in accordance with reported Si photodetectors [21]. The PD2s present different spectral selectivity, displaying a narrow bandwidth response. The corresponding photocurrents of the PD1s have risen, and the PD2s decreased evidently when the Si wafer's thickness rose from 100 to 650 μm. Fig. 2(b) shows the photocurrent ratios of PD1 and PD2 and it can be seen that the ratios gradually rise with the increase of Si thickness from 100 to 650 μm. However, wavelength sensors' UV detection range is sacrificed when the Si thickness is too high. Therefore, selecting a medium and suitable thickness for Si wafer is necessary to assemble the wavelength sensor. Fig. 2(c) and (d) shows the theoretical simulation of dependence on the light angle of incidence using TCAD. It is found that the photocurrent of both devices for all incident light increases when the light angle of incidence increases from 30° to 90° due to relatively small reflected photons at large incident angles [see Fig. 2(c)], which means the photocurrent ratio is affected by the light angle of incidence as well, as shown in Fig. 2(d). In light of this, the vertical incidence would be helpful to avoid the error caused by angle change. What is more, even though silicon's resistivity (doping level) can affect the width of the depletion region in the MSM detector to cause the change of photocurrent [see Fig. 2(e)]. However, no obvious change in the photocurrent ratio was observed, according to our simulation result, shown in Fig. 2(f).

Further experimental photocurrent results of PD1s and PD2s based on Si thicknesses of 100, 200, 480, and 650 μm are shown in Fig. 3(a) (with 5 nm wavelength step). To distinguish from simulation results, calculated photocurrents of PD1 and PD2 are marked as $I_{\mathrm{Ph},1}$ and $I_{\mathrm{Ph},2}$, respectively. The low photocurrents of PD1s and PD2s are magnified on the right side of Fig. 3(a). The tendency is obviously consistent with the theoretical calculation results. And the PD2s are no longer sensitive to the UV range of 265–365 nm when the thickness of the Si wafer increased to more than 200 μm, which is also consistent with the simulated result. Then the photocurrent ratios of PD1 and PD2 were calculated and shown in Fig. 3(b). When the thickness of the Si wafer is too thin (like 100 μm), the UV range of 265–365 nm can be detected, but the functional relationship between $I_{\mathrm{Ph},1}/I_{\mathrm{Ph},2}$ and the light wavelength is nonmonotonic. So it is not suitable for the wavelength sensor. With the increase of thickness, the relationships between the photocurrent ratios and wavelengths obey monotonic functions, making it possible for us to determine the wavelength of the incident light. But the wavelength sensors with 480 and 650 μm Si thicknesses never display a discriminative ability to 265–365 nm irradiation, which means the detection range is limited. Thus, the wavelength sensor based on 200 μm Si shows a more comprehensive detection range than devices composed of other thicknesses

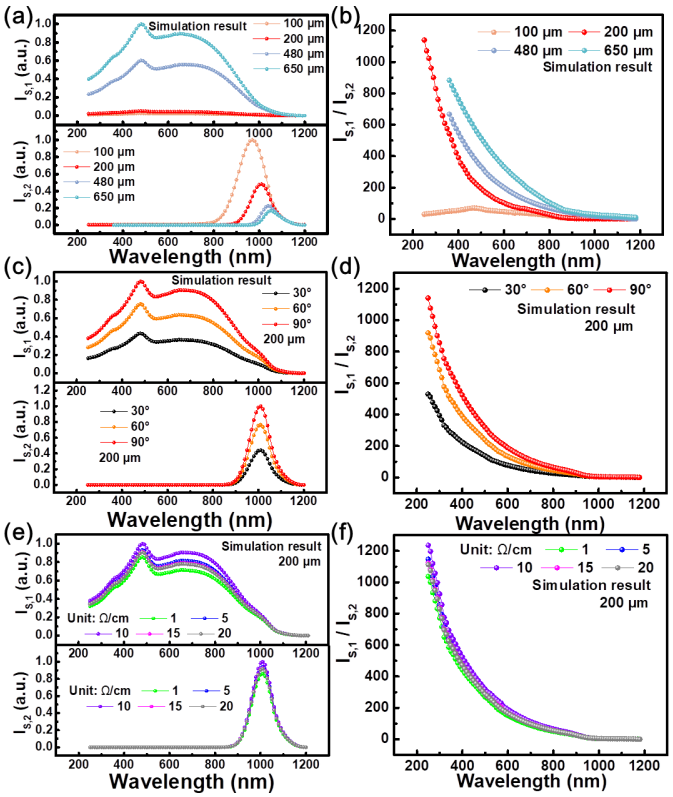

Fig. 2. (a) Current simulation results of the PD1 (top) and the PD2 (bottom) with varying thicknesses in the whole detection range. (b) Simulation photocurrent ratios of the wavelength sensor with different Si thicknesses. (c) Simulation photocurrent of both devices under various light angles of incidence. (d) Simulation photocurrent ratio of the wavelength sensors under various light angles of incidence. (e) Simulation photocurrent of both devices under various resistivity of silicon. (f) Simulation photocurrent ratio of the wavelength sensors under various resistivity of silicon.

of Si. In light of this, 200 μm thickness of Si is selected to assemble the wavelength sensor in the following discussion.

As mentioned above, the Au electrodes can form an excellent Schottky junction with the Si wafer for the present wavelength sensor. However, it will inevitably lead to a typical tradeoff between the Schottky junction and effective illumination areas. For convenience, the finger to a period ratio (η) was equal to gold area to an active area of interdigital electrodes ratio. Here, $\eta = D/(t + D)$, where D and t (t = 200 μm) are the width and gap of interdigital electrodes, respectively [21]. From Fig. 3(c), the experimental results show that the photocurrent ratio increases with the decrease of η at the wavelength range from 265 to 450 nm, reversed at the wavelength more than 450 nm. Moreover, it should be noted that photocurrent ratios are very low at the wavelength of 660–1050 nm, which is not conducive to the distinction of wavelength. As seen from the inset of Fig. 3(c), this trend is improved slightly when η of the wavelength sensor is 50%. Therefore, we chose a 50% gold area of the finger electrode to assemble the wavelength sensor in our work.

To quantitatively assess the optoelectronic performance of both PD1 and PD2 with 200 μm thickness Si and a 50% gold area of the finger electrode, the external quantum efficiency (EQE), responsivity (R), and specific detectivity (D^*) are

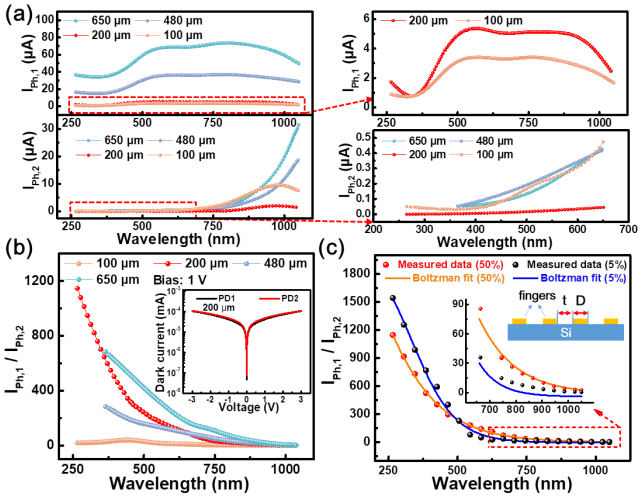

Fig. 3. (a) Spectral response of the PD1 (top) and the PD2 (bottom) of the wavelength sensor with different Si thicknesses in the whole detection range, the light intensity is 1 mW/cm^2. (b) Corresponding photocurrent ratio for the wavelength sensor with different Si thicknesses. Inset: Dark current–voltage curves of two photodiodes. (c) Influence of the finger to a period ratio on the performance of the wavelength sensor.

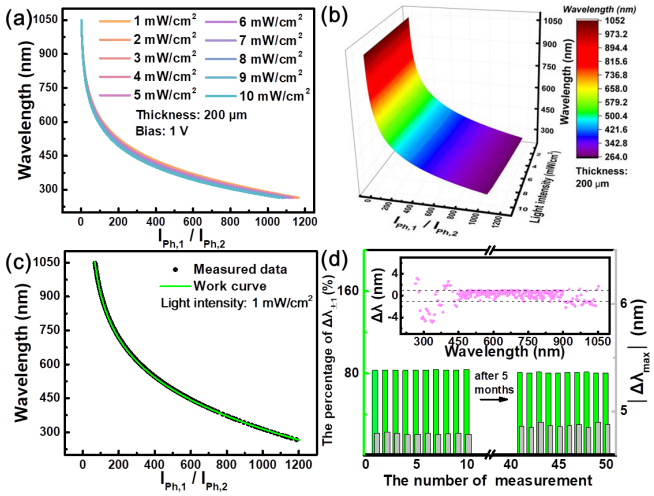

Fig. 4. (a) Wavelength of incident light changes with the photocurrent ratio at different light intensities. (b) Relationship between the photocurrent ratio and the wavelength of the incident light as a function of the light intensity. (c) Experimental validation test of the wavelength detection at fluctuating light intensity of 1 mW/cm^2, and the green curve is the work curve. (d) Study of reproducibility and stability, and after 5 mo of storage in ambient condition. Inset: Comparison of the calculated wavelengths with real wavelengths.

calculated, using the following equation:

$$S = S_{\text{ir}}(1-\eta) \tag{1}$$

$$\text{EQE} = (I_{\text{Ph}}/e)/(PS/h\nu) \tag{2}$$

$$R = I_{\text{Ph}}/(PS) \tag{3}$$

$$D^* = S^{0.5}R/(2eI_d)^{0.5} \tag{4}$$

where S is the effective illumination area, S_{ir} is an irradiated area (0.06 cm^2), a period ratio (η) is 50%, I_{Ph} is the photocurrent, e is the electronic charge, which is 1.602×10^{-19} C, P is the incident light intensity (1 mW/cm^2), h is the Plank's constant (6.626×10^{-34} Js), ν is the frequency of incident light, and I_d is the currents of the device in the dark [22]. Here, the dark current of PD1 and PD2 are 4.23×10^{-5} and 4.82×10^{-5} mA at 1 V bias, respectively [inset of Fig. 3(b)]. Using the photocurrents values in Fig. 3(a), the EQE, R, and D^* under 810 nm wavelength are calculated. The PD1 has a high responsivity of about 0.17 A/W at 1 V, and the EQE is 26.1%. What is more, the detectivity is as high as 2.54×10^{11} Jones. Meanwhile, the R, EQE, and D^* of the PD2 under the same illumination is 0.0068 A/W, 1.04%, and 9.5×10^9 Jones, respectively, which suggests huge difference in photoelectric characteristics when the light is shining from the front (PD1 side). Such differences are due to the unique distribution of photon absorption rate for both PDs [see Fig. 1(b)].

Fig. 4(a) shows the wavelength-photocurrent ratio relationship when shined by light with ten different intensities (1–10 mW/cm^2). As the photocurrent ratio is highly dependent on the light intensity, we systematically fitted the relationship of wavelength-photocurrent ratio at different light intensities using Boltzmann fitting. The relationship can be expressed by the following semiempirical equation that is obtained by numerical fitting:

$$\lambda = A + B\ln\left(\frac{C}{\frac{I_{\text{Ph},1}}{I_{\text{Ph},2}} + D} - 1\right) \tag{5}$$

where λ is the incident light wavelength, and $I_{\text{Ph},1}/I_{\text{Ph},2}$ is the photocurrent ratio. A, B, C, and D are constants that can be affected by the change of detection light intensity. Furthermore, the numerical relationship between light intensity and coefficients A, B, and C are summarized using Boltzmann fitting. Then, the semiempirical equations of these coefficients related to light intensity (P) are obtained by numerical fitting: $A = (648/(1+\exp(P-7.9/2))) - 530$, $B = -7.6\exp((P/8.13) + 140.5$, $C = 341.2\exp(P/1.7) + 4565.5$, $D = 3.5 - 0.039\exp(P/3)$. By introducing light intensity as a new variable, (5) above can be further rewritten as a new semiempirical equation

$$\lambda = \frac{648}{1+\exp\left(\frac{P-7.9}{2}\right)} - 530 + \left(-7.6\exp\left(\frac{P}{8.13}\right) + 140.5\right) \cdot \ln\left(\frac{341.2\exp\left(\frac{P}{1.7}\right) + 4565.5}{\frac{I_{\text{Ph},1}}{I_{\text{Ph},2}} + 3.5 - 0.039\exp\left(\frac{P}{3}\right)} - 1\right) \tag{6}$$

where λ is the incident light wavelength, $I_{\text{Ph},1}/I_{\text{Ph},2}$ is the photocurrent ratio, and P is the light intensity. Using the above function, the relationship of the photocurrent ratios, corresponding light intensity, and wavelength is plotted in Fig. 4(b). That means, once the intensity of the incident light and photocurrent ratio are known, the corresponding wavelength can be easily deduced.

Finally, to explore the reliability of the wavelength sensor in distinguishing wavelengths at a certain light intensity, the experimental results of photocurrent ratios corresponding to wavelengths detection range of 265–1050 nm are plotted in Fig. 4(c), with wavelength step set to be 1 nm. The work curve obtained by (6) is taken as the reference standard as shown in the green curve. It can be seen that the measured data agree well with the work curve. Furthermore, the theoretical wavelengths are calculated by substituting the value of $I_{\text{Ph},1}/I_{\text{Ph},2}$ into the working curve equation, and the known wavelengths are compared. The inset of Fig. 4(d) shows the representative calculation results of 50 measurements. The deviation of the calculated wavelength from the real wavelength is marked

TABLE I
COMPARISON OF OUR DEVICE WITH OTHER WAVELENGTH SENSORS

Device structure	Detection range (nm)	Minimum resolution (nm)	Ref.
Microcavity photodetectors arrays	550-750	1.5	[18]
Colloidal quantum dot spectrometer	400-650	1	[17]
Single-nanowire spectrometers	510-630	8.5	[2]
perovskite photodetectors arrays	450-780	80	[4]
Vertical Si nanowire photodetectors arrays	480-690	5-6	[19]
Buried quad p-n junction photodetector	400-1100	25	[13]
Two photodetectors on an individual Si wafer	**265-1050**	**1**	**This work**

as an absolute error ($\Delta\lambda$). The shift of the wavelength is within ± 1 nm ($\Delta\lambda_{\pm 1}$) for 83.12% of the measurements and within ± 4.8 nm for all measurements. Additionally, a slight fluctuation with the majority in the range of -0.95 to 0.99 nm at wavelengths from 450 to 900 nm, with an average absolute error of ± 0.37 nm. As a reason that a large absolute error of the wavelength sensor in UV range may be caused by unstable light intensity of the UV light source. Moreover, the wavelength sensors exhibited excellent reproducibility and long-term stability. The maximal shift of the wavelength is marked as $\Delta\lambda_{\max}$. The percentage of $\Delta\lambda_{\pm 1}$ and $\Delta\lambda_{\max}$ nearly kept unchanged even after 5 mo of storage in ambient condition. Table I compares the key parameters of our device with other reported wavelength sensors, indicating that previously reported works are not easy to achieve a wide detection range and high resolution at the same time. However, the detection range in this work is improved, from UV to NIR. And the resolution of our wavelength sensor is less than 5 nm when the wavelength intensity is kept at 1 mW/cm^2. In particular, the resolution is as low as 1 nm at the wavelength region from 450 to 900 nm.

IV. CONCLUSION

In summary, we have successfully developed an Au/Si/Au structure wavelength sensor that consists of two photodetectors. The simulation of TCAD shows that the operating principle and detection range of the wavelength sensor are related to both the photo-absorption rate and the thickness of the Si wafer. Further device analysis reveals that the present wavelength sensor has a detection resolution of 5 nm, with a wide detection range from UV (265 nm) to NIR (1050 nm). Especially at the wavelength region from 450 to 900 nm, the resolution is as low as 1 nm. These results provide that the present wavelength sensor may find potential applications in next-generation spectral discrimination systems.

REFERENCES

[1] J. Cong, D. Yan, J. Tang, W. Guo, and X. Mao, "Integrated color photodetectors in 40-nm standard CMOS technology," *IEEE Photon. Technol. Lett.*, vol. 31, no. 24, pp. 1979–1982, Dec. 15, 2019, doi: 10.1109/LPT.2019.2952204.

[2] Z. Yang *et al.*, "Single-nanowire spectrometers," *Science*, vol. 365, no. 6457, pp. 1017–1020, Sep. 2019, doi: 10.1126/science.aax8814.

[3] T.-K. Woodstock and R. F. Karlicek, "RGB color sensors for occupant detection: An alternative to PIR sensors," *IEEE Sensors J.*, vol. 20, no. 20, pp. 12364–12373, Oct. 2020, doi: 10.1109/JSEN.2020.3000170.

[4] H. Sun, W. Tian, X. Wang, K. Deng, J. Xiong, and L. Li, "*in situ* formed gradient bandgap-tunable perovskite for ultrahigh-speed color/spectrum-sensitive photodetectors via electron-donor control," *Adv. Mater.*, vol. 32, no. 14, Apr. 2020, Art. no. 1908108, doi: 10.1002/adma.201908108.

[5] W.-H. Yang *et al.*, "Detection of wavelength in the range from ultraviolet to near infrared light using two parallel $PtSe_2$/thin Si Schottky junctions," *Mater. Horizons*, vol. 8, no. 7, pp. 1976–1984, Jul. 2021, doi: 10.1039/D1MH00286D.

[6] U. Khan and M. Sarkar, "Analysis of charge transfer potential barrier in pinned photodiode of CMOS image sensors," *IEEE Trans. Electron Devices*, vol. 68, no. 6, pp. 2770–2777, Jun. 2021, doi: 10.1109/TED.2021.3071331.

[7] E. R. Fossum and D. B. Hondongwa, "A review of the pinned photodiode for CCD and CMOS image sensors," *IEEE J. Electron Devices Soc.*, vol. 2, no. 3, pp. 33–43, May 2014, doi: 10.1109/JEDS.2014.2306412.

[8] P. C. Biswas, S. Rani, M. A. Hossain, M. R. Islam, and J. Canning, "Recent developments in smartphone spectrometer sample analysis," *IEEE J. Sel. Topics Quantum Electron.*, vol. 27, no. 6, pp. 1–12, Nov. 2021, doi: 10.1109/JSTQE.2021.3075074.

[9] A.-M. Cailean, B. Cagneau, L. Chassagne, M. Dimian, and V. Popa, "Novel receiver sensor for visible light communications in automotive applications," *IEEE Sensors J.*, vol. 15, no. 8, pp. 4632–4639, Jun. 2015, doi: 10.1109/JSEN.2015.2425473.

[10] K. Liang, C. W. Chow, and Y. Liu, "RGB visible light communication using mobile-phone camera and multi-input multi-output," (in eng), *Opt. Exp.*, vol. 24, no. 9, pp. 8–9383, May 2016, doi: 10.1364/oe.24.009383.

[11] I. Dursun *et al.*, "Perovskite nanocrystals as a color converter for visible light communication," *ACS Photon.*, vol. 3, no. 7, pp. 1150–1156, May 2016, doi: 10.1021/acsphotonics.6b00187.

[12] H.-C. Wang, F.-Y. Chang, T.-M. Tsai, C.-H. Chen, and Y.-Y. Chen, "Development and clinical trial of a smartphone-based colorimetric detection system for self-monitoring of blood glucose," *Biomed. Opt. Exp.*, vol. 11, no. 4, pp. 2166–2177, Apr. 2020, doi: 10.1364/BOE.389638.

[13] S. Feruglio *et al.*, "A CMOS buried quad p-n junction photodetector model," *IEEE Sensors J.*, vol. 16, no. 6, pp. 1611–1620, Mar. 2016, doi: 10.1109/JSEN.2015.2501347.

[14] S. H. Kong, D. D. L. Wijngaards, and R. F. Wolffenbuttel, "Infrared micro-spectrometer based on a diffraction grating," *Sens. Actuators A, Phys.*, vol. 92, nos. 1–3, pp. 88–95, Aug. 2001, doi: 10.1016/S0924-4247(01)00544-1.

[15] K. Kumar, H. Duan, R. S. Hegde, S. C. W. Koh, J. N. Wei, and J. K. W. Yang, "Printing colour at the optical diffraction limit," *Nature Nanotechnol.*, vol. 7, no. 9, pp. 557–561, Sep. 2012, doi: 10.1038/NNANO.2012.128.

[16] R. Lukac and K. N. Plataniotis, "Color filter arrays: Design and performance analysis," *IEEE Trans. Consum. Electron.*, vol. 51, no. 4, pp. 1260–1267, Nov. 2005, doi: 10.1109/TCE.2005.1561853.

[17] J. Bao and M. Bawendi, "A colloidal quantum dot spectrometer," *Nature*, vol. 523, no. 7558, pp. 67–70, Jul. 2015, doi: 10.1038/nature14576.

[18] Z. Wang *et al.*, "Single-shot on-chip spectral sensors based on photonic crystal slabs," *Nature Commun.*, vol. 10, p. 1020, Mar. 2019, doi: 10.1038/s41467-019-08994-5.

[19] J. Meng, J. J. Cadusch, and K. B. Crozier, "Detector-only spectrometer based on structurally colored silicon nanowires and a reconstruction algorithm," *Nano Lett.*, vol. 20, no. 1, pp. 320–328, Dec. 2019, doi: 10.1021/acs.nanolett.9b03862.

[20] L. Wang, H. Luo, H. Zuo, J. Tao, and L. Luo, "Highly sensitive narrowband Si photodetector with peak response at around 1060 nm," *IEEE Trans. Electron Devices*, vol. ED-67, no. 99, pp. 1–4, Aug. 2020, doi: 10.1109/TED.2020.3001245.

[21] S. Averine, Y. Chan, and Y. Lam, "Geometry optimization of interdigitated Schottky-barrier metal-semiconductor-metal photodiode structures," *Solid-State Electron.*, vol. 45, no. 3, pp. 441–446, Oct. 2001, doi: org/10.1016/S0038-1101(01)00017-X.

[22] L. Shi *et al.*, "Status and outlook of metal–inorganic semiconductor–metal photodetectors," *Laser Photon. Rev.*, vol. 15, no. 1, Jan. 2021, Art. no. 2000401, doi: 10.1002/lpor.202000401.